Contents lists available at ScienceDirect

Optics Communications

journal homepage: www.elsevier.com/locate/optcom

Residual network-based aberration correction in a sensor-less adaptive optics system

Wei Liu [a], Xinyang Ma [a], Dairan Jin [a], Wenxiao Shi [a], Haijun Gu [a], Jingtai Cao [a,b,*]

[a] *College of Communication Engineering, Jilin University, 5372 Nanhu Road, Changchun 130012, PR China*
[b] *Changchun Institute of Optics, Fine Mechanics and Physics, Chinese Academy of Sciences, 3888 Nanhu Road, Changchun 130033, PR China*

ABSTRACT

The performance of free-space optical communication (FSOC) is often affected by atmospheric turbulence. The sensor-less adaptive optics (SLAO) system is an effective method for overcoming the effects of atmospheric turbulence. The performance of the control algorithm in the SLAO system directly determines whether the SLAO system can effectively correct wavefront aberrations. In this study, we introduce a residual network (ResNet) as a control algorithm to replace the traditional control algorithm. By lowering the number of iterations, this strategy enhances the real-time performance of the FSOC system. The final ResNet model can achieve an accuracy of 0.98 for training and 0.92 for testing. The simulation results show that stochastic parallel gradient descent (SPGD) algorithm takes 700 times longer and requires at least 500 iterations to achieve the same performance as ResNet. And we verify the feasibility of the ResNet model by setting up an experiment.

1. Introduction

Free-space optical communication (FSOC) has been shown to be an effective wireless communication method in recent years [1]. Because compared with other communication systems, the FSOC system has a faster transmission speed and a greater bandwidth. In addition, it is less expensive and easier to install. However, atmospheric turbulence has a significant impact on the performance of an FSOC system. Turbulence-induced wavefront phase aberrations significantly increase the bit error rate (BER) and reduce the mixing efficiency (ME) of the FSOC [2–4].

Adding an adaptive optics (AO) unit to the FSOC system is an effective method for overcoming the effects of atmospheric turbulence [5,6]. The three components of a traditional AO system are the wavefront sensor, wavefront controller, and wavefront corrector. Wavefront aberrations produced by air turbulence can be measured using a wavefront sensor. The wavefront controller regulates the wavefront corrector based on wavefront aberrations measured by the wavefront sensor. The wavefront corrector is responsible for wavefront correction [7].

At present, the sensor-less adaptive optics (SLAO) system is more popular than traditional AO units in optical communication research. Many wavefront-free sensing methods have been widely studied and applied. For example, wavefront sensing algorithms based on random amplitude mask and phase retrieval methods and wavefront sensing methods based on a spatial light modulator (SLM) and an incremental binary random sampling (IBRS) algorithm [8,9]. These methods can be applied in the fields of digital microscopy, aberration correction

and surface contouring. In addition, wavefront-free sensing based on the orbital angular momentum (OAM) multiplexing technique is one of the hot research topics. For example, the use of the SPGD algorithm based on Zernike polynomials to generate phase correction maps for distorted orbital angular momentum beams can effectively improve OAM beam quality and reduce modal crosstalk; The use of the de-focus measurement aided adaptive optics technique, and the use of the random-amplitude mask-based adaptive optics technique is effective in reducing turbulence effects in OAM-based underwater wireless optical communication systems and improving communication quality [10,11]. In addition, wavefront-free sensing techniques based on iterative algorithms and deep learning algorithms are widely studied and applied in the FSOC field [12]. The SLAO system is mainly composed of a charge-coupled device (CCD) high-speed capture camera, wavefront processor, and wavefront corrector. The SLAO system replaces the traditional wavefront sensor with a CCD camera, significantly reducing the cost of building a system [13].

The control algorithm is critical for SLAO systems. The performance of the control algorithm determines whether the SLAO system can successfully suppress the effects of atmospheric turbulence [14]. Therefore, control algorithms have become a key research topic in recent years. The SPGD algorithm, simulated annealing (SA) algorithm, and hill-climbing algorithm are the most commonly used algorithms in SLAO systems [6]. Because of its high correction performance, the SPGD method is the most widely used algorithm in the SLAO system,

although it also has significant drawbacks. For example, the SPGD algorithm easily falls into a local optimum when solving problems, and still needs to iterate many times to reach the goal. Atmospheric turbulence changes continuously; therefore, the SLAO system requires a faster correction speed and higher correction quality [15–17].

Convolutional neural networks (CNNs), which are part of machine learning methods based on learning data representations, have sparked a revolution in artificial intelligence [18]. Recently, studies have applied deep learning methods in adaptive optics. In [14], Tian et al. applied a deep neural network to the AO unit of the FSOC system, which improved the system's real-time performance; However, due to the small capacity of the model with only seven convolutional layers, the final training loss value was as low as 1.88. It resulted in sub-optimal system communication performance [14]. In [13], Gu et al. mixed CNN and SPGD as control algorithms. They rely on the search algorithm to compensate for the distortion, and the neural network is used to measure wavefront aberrations and reduce the search scope. Although the number of iterations is reduced by narrowing the scope through CNN, the current methods still have certain deficiencies for the SLAO system with high real-time requirements.

In the previous study, we applied the hybrid algorithm combining the SA and SPGD algorithm to the SLAO system. We analysed the influence of the hybrid algorithm on the SLAO system. The simulation results show that the hybrid algorithm can effectively improve the wavefront correction capability of the SLAO system. The Ref. [6] is the article published after we summarized the results. The hybrid algorithm performs well in wavefront correction as the control algorithm of the SLAO system but has an average performance in real time. Therefore, in this study, we propose a residual network (ResNet)-based algorithm as a wavefront correction method for SLAO systems. The ResNet is the most representative of Convolutional neural networks, which were proposed by the team of Kaiming He in 2015 [19]. The model shows excellent performance in deep neural network training. The ResNet was introduced as the control algorithm to reduce iterations and improve the real-time performance of the FSOC system in this study. In the experiment, the training accuracy of the ResNet model was 0.98 with a training loss of 0.19, while the testing accuracy was 0.92 with a testing loss of 0.25. Through the experiment and simulation analysis, the real-time performance of the ResNet-based SLAO system has been greatly improved under the premise of ensuring the system's performance.

The remainder of the paper is arranged as follows: Section 2 introduces the principles of the ResNet-based SLAO system; in Section 3, we introduce the three important evaluation indicators and the ResNet model; Sections 4.1 and 4.2 introduce the processing of the dataset and training network in the experiments, Section 4.3 compares the performance of the far-field speckle image before and after correction to demonstrate the wavefront correction performance of the ResNet-based SLAO system; in Section 5, We introduce the composition of the experimental platform, the process of the experiment and the analysis of the experimental results; finally, we discuss the results and conclude the paper in Section 6.

2. ResNet-based SLAO system

Fig. 1 shows the schematic diagram of the FSOC system with its SLAO system for compensating atmospheric turbulence [20]. The photoelectric converter converts the input electrical signal into an optical signal for transmission, and then the SLAO system corrects the optical signal passing through the atmospheric channel. The corrected optical signal is combined with the local oscillator (LO) laser beam, linked and transmitted over single-mode fibre. After that, the photoelectric converter outputs a digital signal from the associated optical signal.

However, during transmission, atmospheric turbulence distorts the wavefront and the amplitude of the laser beam. Therefore, we introduced the SLAO system for atmospheric compensation. The SLAO system consists of a deformable mirror (DM), charge-coupled device

(CCD) camera, and wavefront controller. The CCD obtains the distortion information of the laser beam and then transmits the information to the wavefront controller. According to the distortion information, the wavefront controllers adjust the DM in real time to correct any wavefront aberration. The wavefront controller is an essential component of the SLAO system. The wavefront controller operation is separated into two steps. First, a CCD picture is utilized as input, and then the trained ResNet model is used to categorize wavefront aberration by classifying the picture. Second, based on this categorization, the output voltage controller generates control signals. Thus, the SLAO system can effectively improve the quality of the optical signals after correction.

3. Theoretical basis

3.1. Evaluation indicator

In free-space optical communication, the ME, coupling efficiency, and BER are three important evaluation indicators when evaluating optical communication quality. In the previous study, we applied the hybrid algorithm combining the SA and SPGD algorithm to the SLAO system and analysed the influence of the hybrid algorithm on the coupling efficiency, ME, and BER of the SLAO system. In this study, we use its theoretical basis to evaluate the performance of the SLAO model based on the ResNet algorithm [6,21]. In the following, we will list the calculation formula of the three evaluation indexes and the meaning of the parameters in the formula.

In the focal plane, we calculate the coupling efficiency according to the optical fibre focal plane light field and the incident light focal plane light field. This can be expressed as [22,23]

$$\eta_c \infty \frac{\left| \iint A_f(r) M_0^*(r) d^2r \right|^2}{\iint A_f(r) A_f^*(r) d^2r \times \iint M_0(r) M_0^*(r) d^2r} \quad (1)$$

where $A_f(r)$ is the Fourier transform of the optical fibre mode field, and $M_0(r)$ is the focal plane light field of the incident light.

We assumed the local oscillation is a plane wave, and the intensity of the optical signal (OS) is uniform. In homodyne detection, ME can be defined as [3]

$$\eta = \frac{\left[\int_S A_S A_O \cos(\Delta\varphi) ds \right]^2}{\int_S A_S^2 ds \int_S A_o^2 ds} \quad (2)$$

where A_S and A_O are the amplitudes of the OS and LO, respectively, and $\Delta\varphi$ is the phase difference between the LO and OS.

The BER is one of the most important parameters for evaluating transmission efficiency. For the homodyne detection system, BER can be expressed as [24]

$$BER = \frac{1}{2} erfc\left(\sqrt{2\delta N_P \eta}\right) \quad (3)$$

where N_P represents the number of photons received in a single bit, δ denotes the quantum efficiency of the detector, *erfc* is the complementary, and η is the mixing efficiency of coherent FSOC system.

3.2. ResNet model

Compared with other convolutional neural networks, the ResNet can successfully address network deepening-induced gradient expansion and gradient disappearance in neural networks. It is mainly composed of a series of residual blocks, whose basic structural units are shown in Fig. 2. ResNet mainly consists of two parts: the direct mapping and the residual parts. The direct mapping part directly connects the input and output of the residual block. The residual part is an identity mapping layer superimposed on a shallow network, with input x and expected output H(x). In addition, F(x) = H(x) − x is the difference between the input and output of the learning target of the ResNet, that is, the residual. The training of F(x) is more straightforward than that of H(x), and it can also amplify the weak changes, avoiding the problem
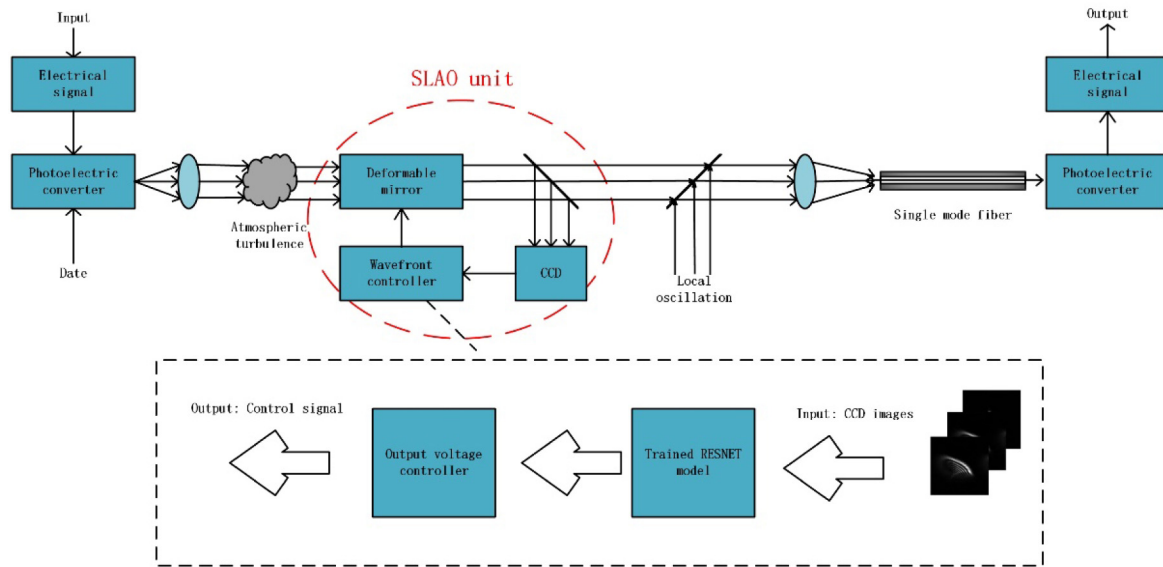
Fig. 1. Schematic diagram of the FSOC system.
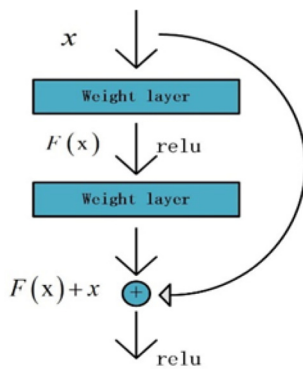

Fig. 2. Basic structural unit of the residual block.

of gradient disappearance and gradient explosion [19]. The ResNet is able to train deeper network models with greater capacity and more convolutional layers than CNN and DNN, and therefore also enables better training results with the better fitting of the objective function.

4. Numerical simulation and discussion

4.1. Data generating and pre-processing

The dataset is critical in training a ResNet model, and the quality of the dataset directly influences the quality of the trained model. Table 1 shows the expression for the Zernike polynomials involved. The wavefront aberration information that affects the communication performance of FSOC systems is mainly concentrated in the lower-order part of the Zernike aberration [25]. Among them, defocus aberration is crucial for communication performance in the FSOC system. Therefore, we place the fourth aberration in the large-scale dimension. Meanwhile, too many categories would increase the number of model parameters, making training more difficult and reducing the accuracy of the model. Therefore, we chose categories with the following Zernike coefficients.

$a4 \in [-1.5, -1.0) \cup [-1.0, -0.5) \cup [-0.5, 0] \cup (0, 0.5] \cup (0.5, 1.0] \cup (1.0, 1.5]$

$a5, a6 \in [-1.0, -0.5) \cup [-0.5, 0] \cup (0, 0.5] \cup (0.5, 1.0]$

$a7, a8, a9 \in [-0.5, 0] \cup (0, 0.5]$

Wavefront aberrations are classified into $6 \times 4 \times 4 \times 2 \times 2 \times 2 = 768$ types, with each type of wavefront aberration corresponding to a different subspace. We established a standard for each subspace. The standard factor was defined as the median of the range of coefficients for each classification. In this way, every image captured by the CCD camera can be classified into one of these categories. However, because of the defocus mode, the point spread functions are similar for both positive and negative cases with the same absolute value [26]. Therefore, we divided 768 wavefront aberrations into two major categories in our experiments: 384 wavefront aberrations for positive out-of-focus modes and 384 wavefront aberrations for negative out-of-focus modes. This method can reduce the types of wavefront aberrations and improve the accuracy of the model. In our experiments, we used a dataset consisting of 384 classes of wavefront aberrations for the case where the defocus mode was positive; 422 400 photos were created at random, with 1000 images in each category serving as the training set and 100 images serving as the test set. In practice, we can train the algorithmic model for the negative defocus mode using the same technique as that used for the positive defocus mode. The two models in the wavefront control unit categorize the input point spread function concurrently and then choose the best compensated classification.

In this paper, we refer to the far-field spot generation approach in the literature [27], which is divided into two main steps. Firstly, the phase matrix is generated from the Zernike coefficients. In the second step, the phase matrix is transformed into the image matrix of the far-field spot through a two-dimensional Fourier transform. The two-dimensional Fourier transform is given by

$$F(u, v) = \int_{-\infty}^{\infty} \int_{-\infty}^{\infty} f(x, y) e^{-j2\pi \left(\frac{ux + vy}{dl} \right)} dx dy \qquad (4)$$

where $f(x, y)$ represents the wavefront phase matrix generated by the Zernike coefficients, $F(u, v)$ represents the resulting image matrix, d is the equivalent interval of the actuator interval projected on the entrance pupil of the receiving antenna, l is the signal wavelength.

In this study, we performed the training of the ResNet on a high-performance personal computer. The CPU model was i7 8700, the main frequency was 3.70 GHz, the system memory size was 64 GB, and the GPU used two GTX1080Ti to train the model to improve efficiency.

4.2. Model setting and evaluation

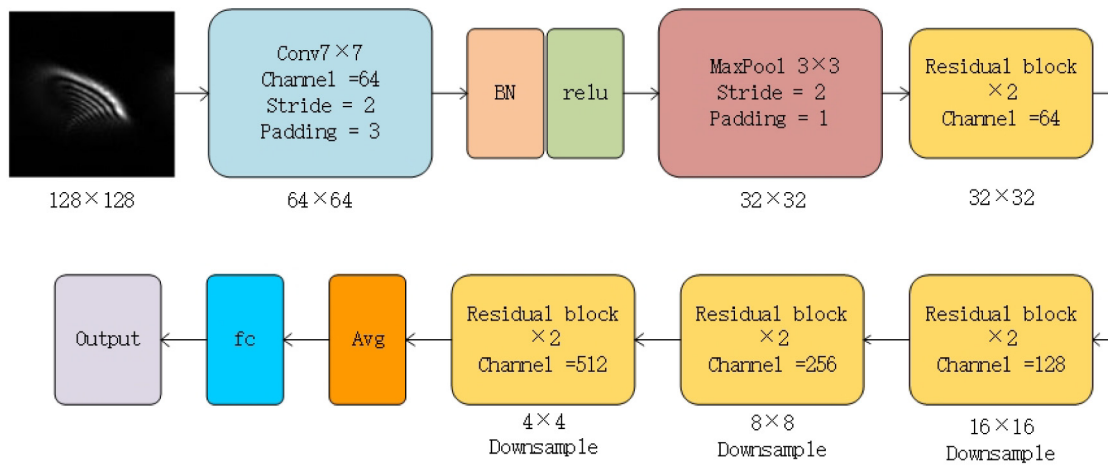In the experiment, the network model we used was ResNet20, whose structure is shown in Fig. 3.

Fig. 3. Basic structural unit of the ResNet.

Table 1
Expression of $k = 4 - 9$ order of Zernike polynomial.

k	(n,m)	Polar coordinates	Mode
4	(2,0)	$\sqrt{3}\left(2\rho^2 - 1\right)$	Defocus
5	(2,−2)	$\sqrt{6}\rho^2 \sin 2\theta$	Astigmatism
6	(2,2)	$\sqrt{6}\rho^2 \cos 2\theta$	Astigmatism
7	(3,−1)	$2\sqrt{2}\left(3\rho^3 - 2\rho\right)\sin\theta$	Coma
8	(3,1)	$2\sqrt{2}\left(3\rho^3 - 2\rho\right)\cos\theta$	Coma
9	(3,−3)	$2\sqrt{2}\rho^3 \sin 3\theta$	Trefoil

This table shows θ = polar coordinate angle and ρ = radius (normalized to 1 at the edge of the aperture). The numbers in columns m and n are the indices for Zernike polynomials.

Fig. 4. Curve of learning rate attenuation.

In Fig. 3, Batch Normalization (BN) and rectified linear unit (relu) are often combined with speeding up the convergence of the model during training, making the training process more stable and avoiding gradient explosion or gradient disappearance. Finally, the classification results were obtained using average pooling (Avg) and a dimensional full connection layer (fc). The figure is labelled with the change in image size.

In model training, adjusting the hyperparameters is an important part of the experiment. Among them, the learning rate is an important hyperparameter in deep learning; therefore, its adjustment is vital [28]. In general, an excessive learning rate causes failure of model training convergence, and the trained model is not accurate. However, if the learning rate is too low, the model converges slowly and easily falls into the local optimal solution. A suitable learning rate can make the model converge to the minimum value within a suitable time. Therefore, in the actual model training, the learning rate is not a fixed value, and it takes the way of continuous attenuation to improve the training performance to the greatest extent. The common decay methods of learning rate are the exponential descent method, fixed step decay method, multi-step decay method, and cosine annealing decay method. Among them, the exponential decay method is mainly used for network models that are easy to train and easy to converge; the fixed step decay method converges faster, but it is easy to fall into local optimal solutions during the training process; the cosine annealing decay method avoids falling into local optimal solutions by warm restart, but this decay method is more suitable for the case where there are multiple locally optimal solutions in the optimization process of the objective function. We have therefore chosen the multi-step decay method. The advantage of the decay method is that the step size and learning rate can be adjusted according to the specific situation in the model training, ensuring fast convergence while effectively avoiding falling into a local optimum solution. The specific values of the learning rate decaying with epoch are shown in Fig. 4. Epoch defines the number of times the learning
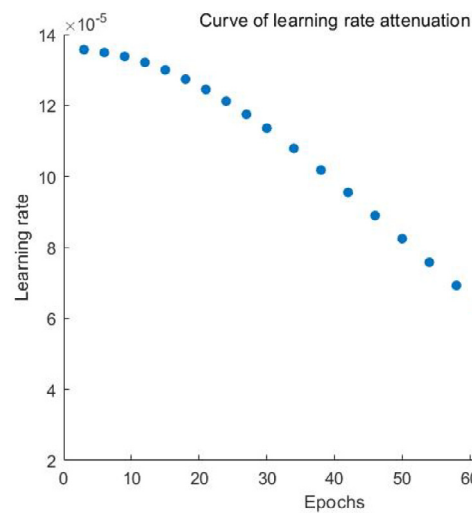
algorithm works on the entire training data set. An epoch represents one complete model training using all the data from the training set. The final model accuracy rate trained by the experiment is shown in Fig. 5, and the loss is shown in Fig. 6.

In the training of a model, Accuracy is the ratio of the number of correctly classified samples to the total number of samples, and a higher Accuracy value means a better fit. It can be seen from Fig. 5 that the training and validation accuracy curves exhibit an upward trend with the increase in epochs. The accuracy value of training the accuracy curve increased steadily from 0.63 and stabilized at 0.98 after 70 epochs. The accuracy value of the validation accuracy curve increases from 0.71 to 0.90 after 30 epochs of rapid growth with slight oscillations and reaches 0.92 after 40 epochs of slow growth and gradually stabilizes.

During the training of a model, we usually define an objective function and want to optimize it to the lowest point. These functions are called loss functions. The value of the loss function is the loss value. As the scenario used in this paper is a multi-classification problem, a categorical cross-entropy loss function is used, which can be expressed as follows [29]:

$$Loss = -\sum_{i=1} y_i \cdot \log \hat{y}_i \tag{5}$$

where i denotes the ith output node of the softmax layer. y_i denotes the true distribution of the sample, $\hat{y}_i$ denotes the distribution predicted by
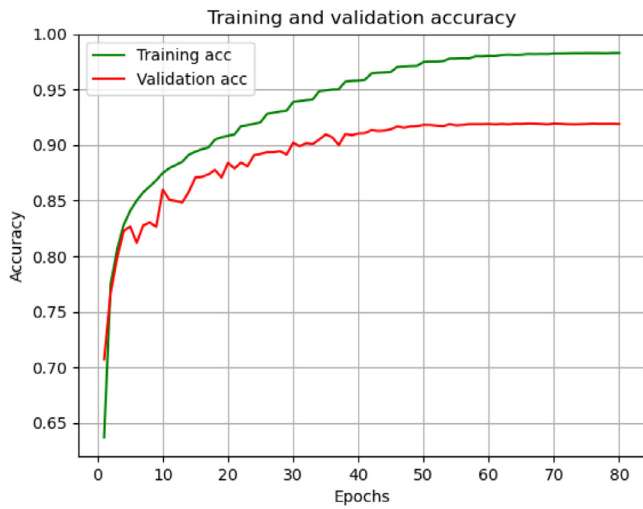
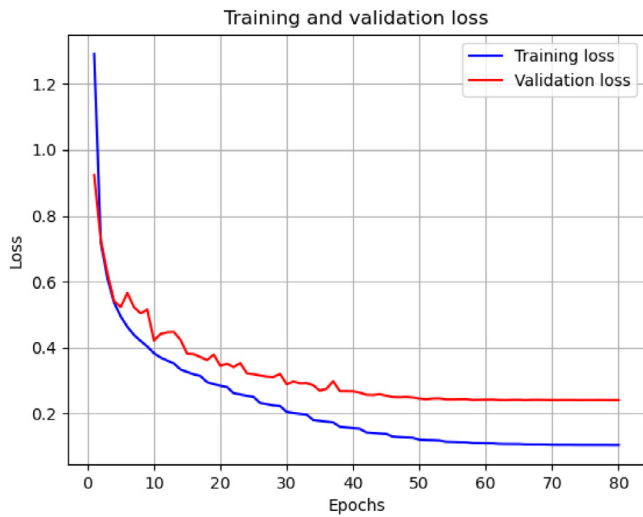**Fig. 5.** Training accuracy and validation accuracy.

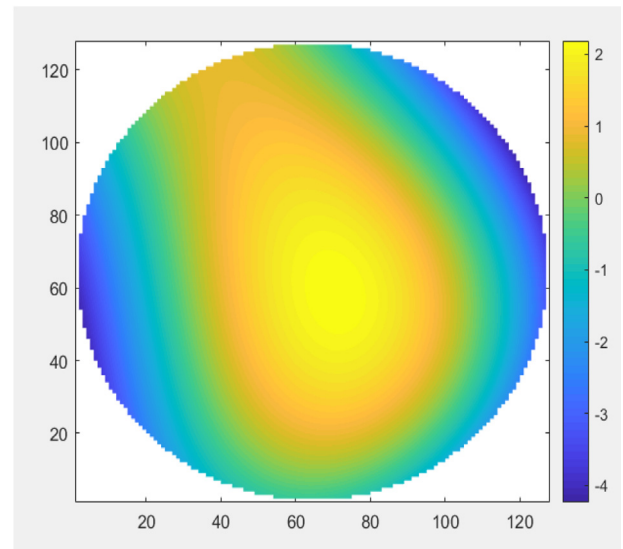**Fig. 6.** Training loss and validation loss.

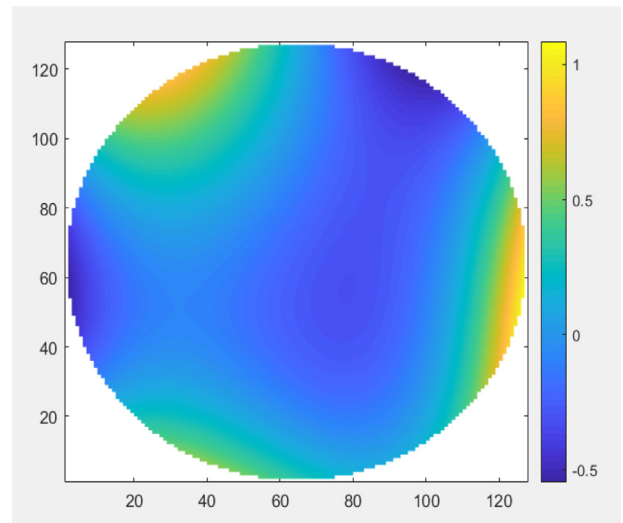**Fig. 7(a).** Phase diagram before correction.

Fig. 7(b). Phase diagram after correction.

the model. From Fig. 6, we can see that the training and validation loss curves show a decreasing trend with an increase in the epoch. The loss value of the training loss curve starts to decrease rapidly from 1.33 and finally stabilizes at 0.19 after 70 epochs; the loss value of the validation loss curve starts to decrease from 0.92 and stabilizes at 0.25 after 60 epochs and slight oscillations.

In our experiment, the training process both works offline. After testing, the model takes only 54 s to test 76,800 images, with an average of 0.0007 s to classify one image. The size of the model is 7.92 MB.

4.3. Numerical simulation

To test the wavefront correction performance of the ResNet-based SLAO system in the FSOC system. We generated 20 far-field light spot images using a generated test set. The trained ResNet model classified them, and wavefront correction was performed based on the classification results. Figs. 7 and 8 show some of the far-field spot pictures and phase diagrams before and after correction.

A comparison of the before and after correction in Figs. 7 and 8 show that the ResNet-based SLAO system can effectively suppress the wavefront distortion caused by atmospheric turbulence. The horizontal

and vertical coordinates of Fig. 7 represent pixel points, so the image size is 128 pixels by 128 pixels. We also calculated the ME, coupling efficiency, and BER for the 20 images before and after correction to evaluate the correction performance of the SLAO system.

Fig. 9 compares the mixing efficiency of the 20 far-field light spots before and after rectification. Before the correction, the average mixing efficiency of far-field light spots was 0.3871, while after adjustment, the average mixing efficiency of the far-field light spots was 0.9821. Fig. 10 compares the coupling efficiency of the 20 far-field light spots before and after correction. The average coupling efficiency of the far-field light spots before the correction was 0.4517, and the average value after the correction was 0.8008. It is also worth noting that, after correction, the system's coupling efficiency is close to a maximum of 0.81 for single-mode fibre coupling efficiency. Fig. 11 compares bit error rates for 20 far-field spots before and after rectification. The far-field spots had an average bit error rate of 4.266E−03 before the correction and an average value of 1.898E−10 after the correction. Figs. 9–11 show that, before correction, in the 20 far-field spot pictures, Nos. 1 and 5 are considerably influenced by air turbulence, but Nos. 7 and
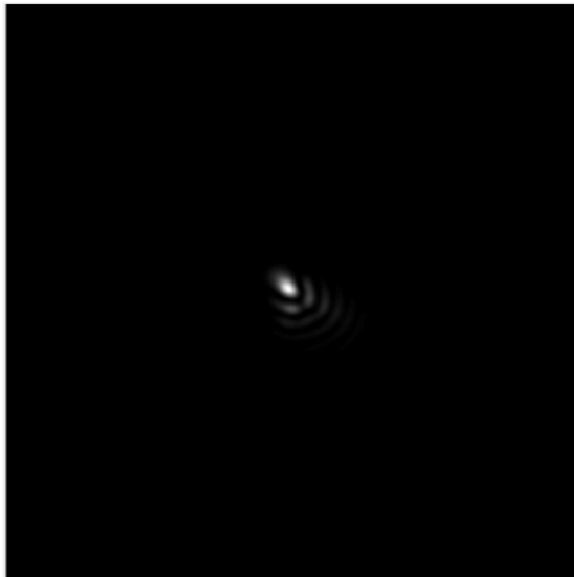
Fig. 8(a). Far-field spot before correction.

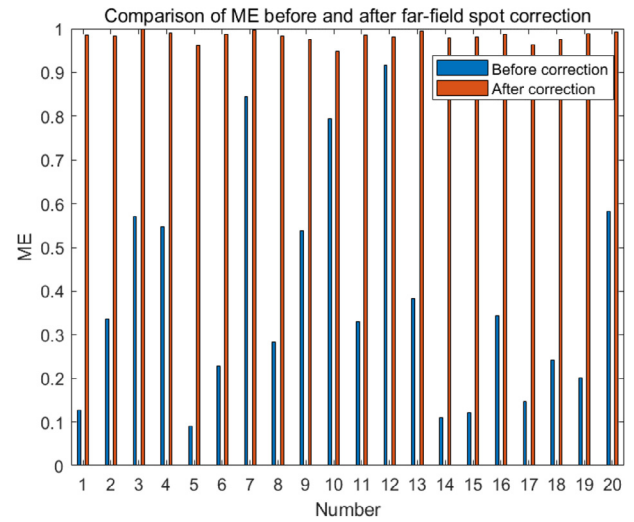**Fig. 8(b).** Far-field spot after correction.

Fig. 9. Comparison of ME before and after far-field spot correction.
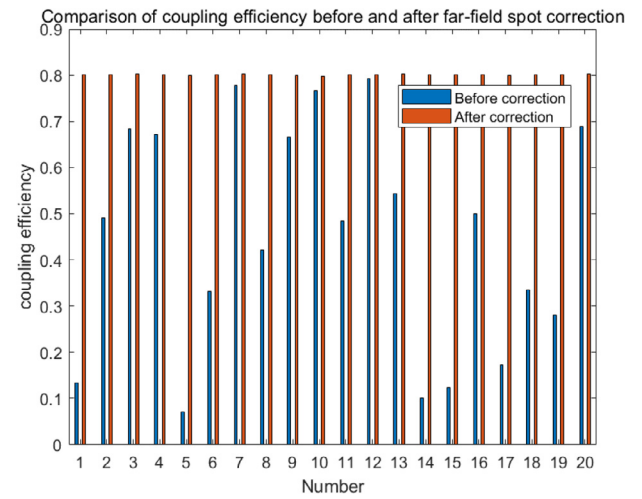

Fig. 10. Comparison of coupling efficiency before and after far-field spot correction.

Table 2

Main equipment in the experiment and its key parameters.

Control method	Latency (ms)
ResNet	0.7
DNN	2
CNN3	6–7
hybrid algorithm (CNN and SPGD)	100–150
SPGD	300–500

12 are less affected by atmospheric turbulence. However, after the correction, the mixing efficiency can reach more than 0.95, the coupling efficiency can reach more than 0.79, and the BER can be reduced to approximately 1.0E−10. A comparison of the three evaluation indexes before and after the correction shows that the SLAO system based on the ResNet algorithm has high wavefront correction capabilities in the FSOC system and can effectively reduce wavefront distortion induced by atmospheric turbulence. The SLAO system with SPGD as the control algorithm usually requires approximately 500 iterations to achieve the same performance. The ResNet takes just 0.7 ms on average to classify a far-field location, but the SPGD takes approximately 500 ms to iterate 500 times. Compared to the hybrid algorithm in the literature [13], the ME can reach 0.8 after the pre-processing of the CNN and 150 iterations of the SPGD algorithm [13]. But ResNet can achieve the same result in a much shorter time. In addition, ResNet is also able to perform a single correction in less time than SLAO systems that also use convolutional neural networks as their control algorithm, such as DNN and CNN 3

(CNN with 3 convolutional layers) [30]. The time required for a single correction for different control algorithms is presented in Table 2. As a result, ResNet as a control method can significantly increase the real-time performance of the FSOC system.

5. Experiments and results analysis

To further test the performance of the trained ResNet model in wavefront aberration correction, we conducted experiments on the home-built system consisting of a two-stage fast-steering-mirror (FSM) and an AO unit with a 97-element continuous surface deformable mirror (CSDM). The phase-screen used in our experiment was customized by Lexitek corporation. We can simulate the Greenwood frequency by rotating the phase screen, and by adjusting the position of the phase
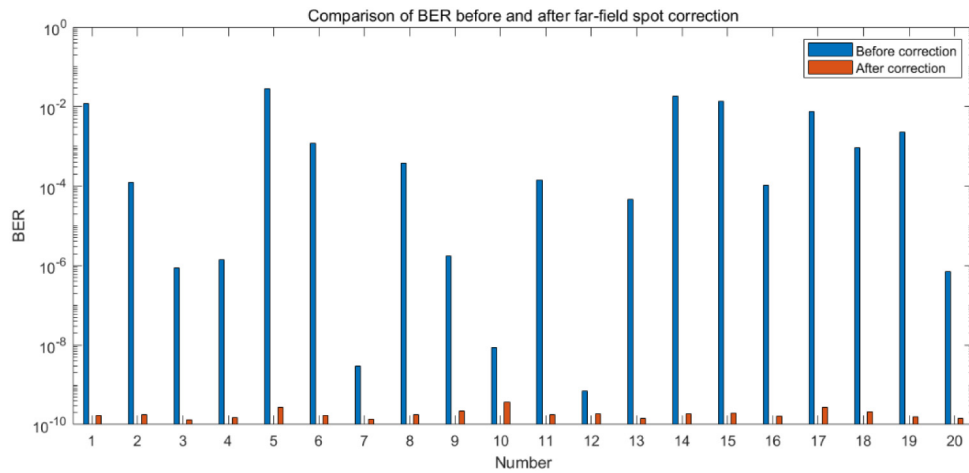
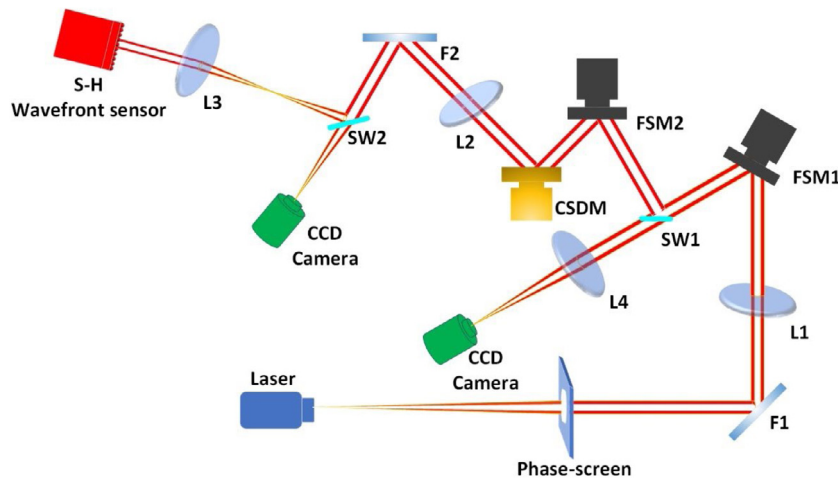**Fig. 11.** Comparison of BER before and after far-field spot correction.

Fig. 12. The schematic diagram of experimental system.

Table 3
Main equipment in the experiment and its key parameters.

Main equipment	Key parameters
S-H wavefront sensor	Wave length is 550 nm
Laser	Wave length is 532 nm
L1	Focal length is 400 nm
L2	Focal length is 3000 nm; aperture is 80 mm
L3	Focal length is 3000 nm
L4	Focal length is 300 nm; aperture is 80 mm
CSDM	Focal length is 200 nm; aperture is 7 mm

Fig. 13. The photo of experimental system.

screen to simulate the r_0. Thus, we can use this phase screen to simulate different atmospheric turbulence intensities. Fig. 12 shows a schematic diagram of the experimental system. In Fig. 12, L1 to L4 are a set of lenses, F1 and F2 represent the reflection mirror, SW1 and SW2 are split wave receivers, and the S-H Wavefront sensor represents the Shack-Hartmann wavefront sensor. Table 3 lists the essential parameters of the experiment's primary apparatus [21]. The photo of the designed experimental system is shown in Fig. 13 [21].

We re-collected a group of experimental data based on the experimental platform. In the experiment, the far-field light spots acquired by the CCD camera could not correspond to the Zernike coefficient generated by the S-H Wavefront sensor one by one because the CCD camera frequency was lower than that of the S-H Wavefront sensor. Therefore, we reconstructed the excess Zernike coefficients into far-field light spots, and then sent them into the trained ResNet model for
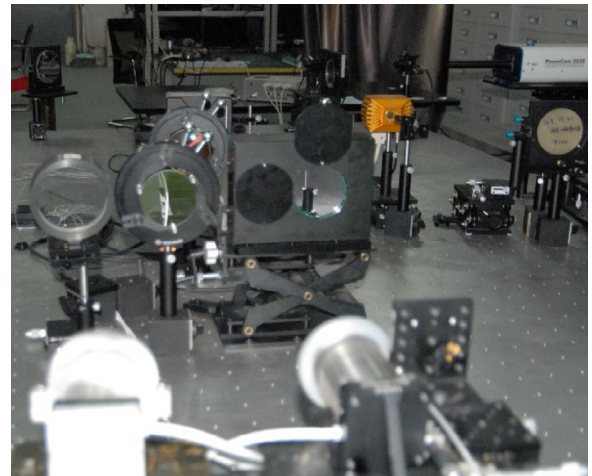
classification. In addition, we added Gaussian noise to the far-field spot generation to simulate the noise produced by CCD camera imaging. To evaluate the effectiveness of the ResNet algorithm, we analysed the ME before and after correction. Measuring the ME of far-field light patches before and after classification was used to test the model's ability.
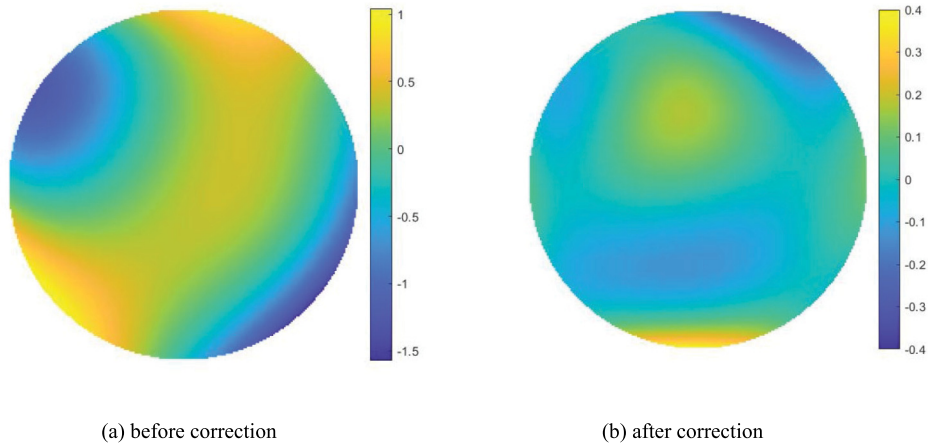
(a) before correction

(b) after correction

Fig. 14. Phase diagram before and after correction.

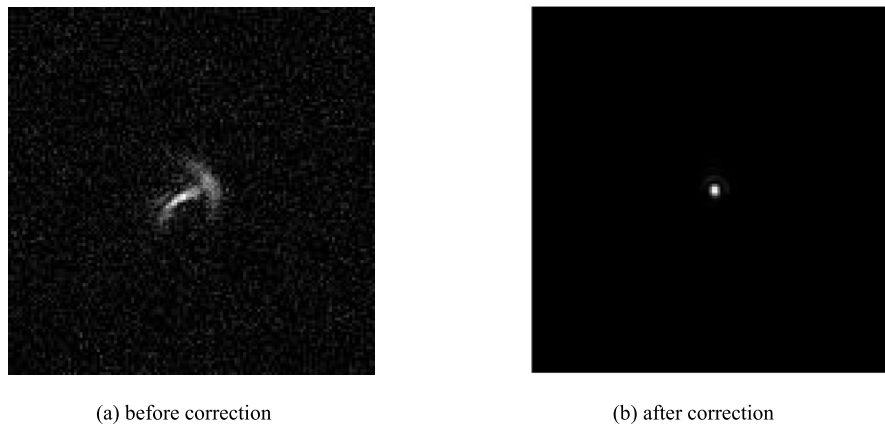(a) before correction

(b) after correction

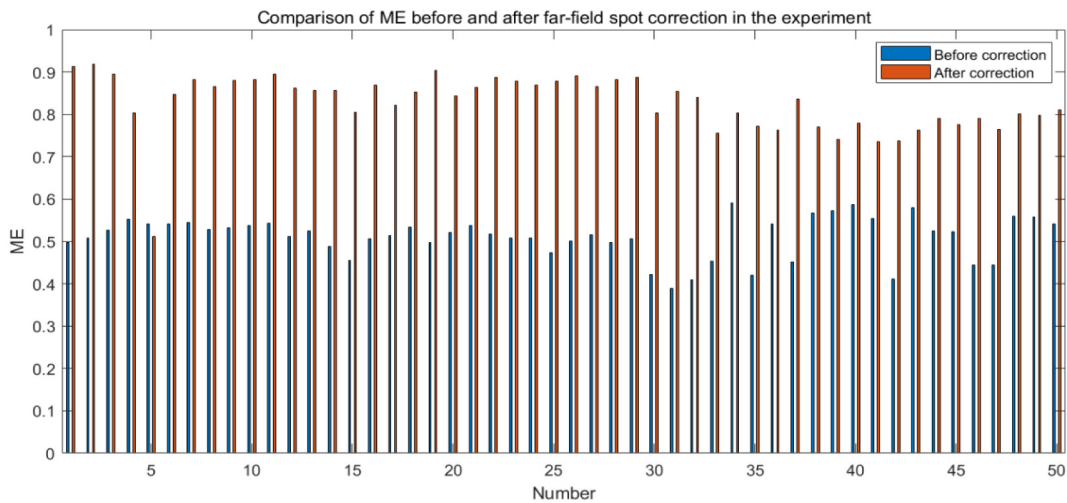**Fig. 15.** Far-field spot before and after correction.

Fig. 16. Comparison of ME before and after far-field spot correction in the experiment.

Figs. 14 and 15 show the phase and far-field spot maps before and after correction in a set of experiments. ME is 0.498 before correction and 0.916 after correction, indicating a good correction impact. Fig. 16 shows part of the data from the experiment. Except for the data in No. 5, the ME of the remaining 49 groups of data can be improved to around 0.8, according to the experimental data. The mean

ME before correction was 0.510 and the mean after correction was 0.833 for all 49 groups except for the fifth group of data. The results show that the ResNet as a control algorithm for the SLAO system can effectively correct wavefront distortion and improve the FSOC system performance. Therefore, we focused our analysis on the data with poor performance. After analysis, we believe when we generated

the dataset, the interval division of the fourth- and fifth-order Zernike coefficients were too widely spaced, resulting in unsatisfactory far-field spot recognition generated for data that were partially at the edge of the interval. The fourth-order Zernike coefficients were mostly clustered in $[-0.8, +0.8]$ among the experimentally obtained Zernike coefficients, and data more than 1 or less than -1 were unusual. The fifth-order Zernike coefficients likewise cluster around $[0.5, 1.0]$ or $[-0.5, -1.0]$. Therefore, the generated far-field spots are relatively similar, which also leads to the reduced classification ability of the model. Therefore, in future work, we will improve the generation of the dataset with a more reasonable regionalization of the fourth- and fifth-order Zernike coefficients.

6. Conclusion

In this study, we applied ResNet as a control algorithm for measuring and correcting the wavefront aberration to the SLAO system of an FSOC system. By training a well-designed ResNet model, this method can acquire the control signal of the DM directly from the CCD images. Compared with our previous studies, this approach can avoid generating iterations and effectively improve the real-time performance of the FSOC system. According to the simulation results, SPGD takes 700 times longer and requires at least 500 iterations to obtain the same performance as ResNet. The control algorithm based on ResNet as the SLAO system can effectively improve the real-time performance of the FSOC system, which has a certain reference value for future FSOC system design. Moreover, we can create more targeted datasets to train the ResNet model offline for different scenarios in real engineering applications to improve the correction performance of the ResNet algorithm. We used a home-built experimental platform to verify the classification ability of the model, and we analysed the experimental results and problems. We believe that dividing the fourth- and fifth-order Zernike coefficient intervals in the dataset used in the training model needs to be improved. In addition, we set up the data set to focus more on the turbulence intensity in weak and medium turbulence. Therefore, how to use ResNet as a control algorithm for wavefront correction under strong turbulence is also one of the main problems we face. A better solution at present is to mix ResNet with traditional algorithms such as SPGD, using traditional control algorithms to deal with the few cases caused by inaccurate classification of ResNet algorithm or strong turbulence interference, and using ResNet to deal with moderate to weak turbulence and most non-special cases. This approach can ensure the real-time performance of the FSOC system and further improve the wavefront correction performance and stability of the system. This is also the main direction of our future work.

Declaration of competing interest

The authors declare that they have no known competing financial interests or personal relationships that could have appeared to influence the work reported in this paper.

Data availability

No data was used for the research described in the article.

Funding

References

[1] Magdalena Garlinska, Agnieszka Pregowska, Karol Masztalerz, Magdalena Osial, From mirrors to free-space optical communication—Historical aspects in data transmission, Future Internet 12 (11) (2020) 179, http://dx.doi.org/10.3390/fi12110179.

[2] Wei Liu, Kainan Yao, Lu Chen, Danian Huang, Jingtai Cao, Haijun Gu, Performance analysis of coherent free space optical communications with sequential pyramid wavefront sensor, Opt. Laser Technol. (ISSN: 0030-3992) 100 (2018) 332–341, http://dx.doi.org/10.1016/j.optlastec.2017.09.030.

[3] Jingtai Cao, Xiaohui Zhao, Wei Liu, Haijun Gu, Performance analysis of a coherent free space optical communication system based on experiment, Opt. Express 25 (2017) 15299–15312.

[4] A. Mansour, R. Mesleh, M. Abaza, New challenges in wireless and free space optical communications, Opt. Lasers Eng. (ISSN: 0143-8166) 89 (2017) 95–108, http://dx.doi.org/10.1016/j.optlaseng.2016.03.027, (https://www.sciencedirect.com/science/article/pii/S0143816616300252).

[5] Xiangyu Fu, Jiafei Fang, Shilin Xiao, Xiaoyu Liu, Lizhuo Zheng, Weisheng Hu, Dual-RNN based polar decoder with tanh-modified LLR over FSO turbulence channel, Opt. Commun. (ISSN: 0030-4018) 527 (2023) 128965, http://dx.doi.org/10.1016/j.optcom.2022.128965.

[6] Wei Liu, Dairan Jin, Wenxiao Shi, Jingtai Cao, Performance analysis of coherent optical communication based on hybrid algorithm, Opt. Laser Technol. (ISSN: 0030-3992) 149 (2022) 107878, http://dx.doi.org/10.1016/j.optlastec.2022.107878.

[7] Xu He, Xiaohui Zhao, Suying Cui, Haijun Gu, A rapid hybrid wave front correction algorithm for sensor-less adaptive optics in free space optical communication, Opt. Commun. (ISSN: 0030-4018) 429 (2018) 127–137, http://dx.doi.org/10.1016/j.optcom.2018.08.008.

[8] Arun Anand, Giancarlo Pedrini, Wolfgang Osten, Percival Almoro, Wavefront sensing with random amplitude mask and phase retrieval, Opt. Lett. 32 (2007) 1584–1586.

[9] Ben-Yi Wang, Lu Han, Yang Yang, Qing-Yang Yue, Cheng-Shan Guo, Wavefront sensing based on a spatial light modulator and incremental binary random sampling, Opt. Lett. 42 (2017) 603–606.

[10] Guodong Xie, Yongxiong Ren, Hao Huang, Martin P.J. Lavery, Nisar Ahmed, Yan Yan, Changjing Bao, Long Li, Zhe Zhao, Yinwen Cao, Moshe Willner, Moshe Tur, Samuel J. Dolinar, Robert W. Boyd, Jeffrey H. Shapiro, Alan E. Willner, Phase correction for a distorted orbital angular momentum beam using a Zernike polynomials-based stochastic-parallel-gradient-descent algorithm, Opt. Lett. 40 (2015) 1197–1200.

[11] L. Zhu, X. Xin, H. Chang, X. Wang, Q. Tian, Q. Zhang, R. Gao, B. Liu, Security enhancement for adaptive optics aided longitudinal orbital angular momentum multiplexed underwater wireless communications, Opt. Express 30 (6) (2022) 9745–9772, http://dx.doi.org/10.1364/OE.453264, PMID: 35299393.

[12] Lei Zhu, Haipeng Yao, Huan Chang, Qinghua Tian, Qi Zhang, Xiangjun Xin, F. Yu, Adaptive optics for orbital angular momentum based internet of underwater things applications, IEEE Internet Things J. (2022) http://dx.doi.org/10.1109/JIOT.2022.3190268.

[13] Haijun Gu, Meiqi Liu, Haoyu Liu, Xue Yang, Wei Liu, An algorithm combining convolutional neural networks with SPGD for SLAO in FSOC, Opt. Commun. (ISSN: 0030-4018) 475 (2020) 126243, http://dx.doi.org/10.1016/j.optcom.2020.126243.

[14] Qinghua Tian, Chenda Lu, Bo Liu, Lei Zhu, Xiaolong Pan, Qi Zhang, Leijing Yang, Feng Tian, Xiangjun Xin, DNN-based aberration correction in a wavefront sensorless adaptive optics system, Opt. Express 27 (2019) 10765–10776.

[15] J. Li, J. Luo, Z. Xu, X. Yuan, Experimental study on wavefront distortion correction of 40-elements adaptive optical system based on SPGD algorithm, in: 2020 IEEE/CIC International Conference on Communications in China (ICCC Workshops), 2020, pp. 248–252, http://dx.doi.org/10.1109/ICCCWorkshops49972.2020.9209914.

[16] Yu Zhang, Xiaobo Tian, Rongguang Liang, SPGD and Newton iteration mixed algorithm used in freeform surface metrology, Opt. Lasers Eng. (ISSN: 0143-8166) 129 (2020) 106050, http://dx.doi.org/10.1016/j.optlaseng.2020.106050.

[17] Yunhan Wu, Shuai Shao, Yixuan Li, Xiangzheng Chen, Dongbo Che, Jiayu Chen, Kunyang Du, Ruitao Jiang, Xunqing Huang, Dongping Kan, Multi-beam optical phase array for long-range LiDAR and free-space data communication, Opt. Laser Technol. (ISSN: 0030-3992) 151 (2022) 108027, http://dx.doi.org/10.1016/j.optlastec.2022.108027.

[18] Ke Yu, Jing He, Zheng Huang, Decoding scheme based on CNN for mobile optical camera communication, Appl. Opt. 59 (2020) 7109–7113.

[19] H. Yoo, S. Han, K. Chung, Diagnosis support model of cardiomegaly based on CNN using ResNet and explainable feature map, IEEE Access 9 (2021) 55802–55813, http://dx.doi.org/10.1109/ACCESS.2021.3068597.

[20] Wei Liu, Kainan Yao, Danian Huang, Xudong Lin, Liang Wang, Yaowen Lv, Performance evaluation of coherent free space optical communications with a double-stage fast-steering-mirror adaptive optics system depending on the Greenwood frequency, Opt. Express 24 (2016) 13288–13302.

[21] W. Liu, K. Yao, D. Huang, X. Lin, L. Wang, Y. Lv, Performance evaluation of coherent free space optical communications with a double-stage fast-steering-mirror adaptive optics system depending on the greenwood frequency, Opt. Express 24 (2016) 13288–13302.

[22] Peter J. Winzer, Walter R. Leeb, Fiber coupling efficiency for random light and its applications to lidar, Opt. Lett. 23 (1998) 986–988.

[23] Yamaç Dikmelik, M. Frederic, Davidson, fiber-coupling efficiency for free-space optical communication through atmospheric turbulence, Appl. Opt. 44 (2005) 4946–4952.

[24] J. Cao, X. Zhao, W. Liu, et al., BER analysis of coherent free-space optical communication systems with a focal-plane-based wavefront sensor, J. Korean Phys. Soc. 72 (2018) 555–560, http://dx.doi.org/10.3938/jkps.72.555.

[25] Gleb Vdovin, Oleg Soloviev, Alexander Samokhin, Mikhail Loktev, Correction of low order aberrations using continuous deformable mirrors, Opt. Express 16 (2008) 2859–2866.

[26] Yuncheng Jin, Yiye Zhang, Lejia Hu, Haiyang Huang, Qiaoqi Xu, Xinpei Zhu, Limeng Huang, Yao Zheng, Hui-Liang Shen, Wei Gong, Ke Si, Machine learning guided rapid focusing with sensor-less aberration corrections, Opt. Express 26 (2018) 30162–30171.

[27] J.W. Goodman, Introduction to Fourier Optics, Roberts and Company Publishers, 2005.

[28] Nakamura Kensuke, Bilel Derbel, Kyoung-Jae Won, Byung-Woo Hong, Learning-rate annealing methods for deep neural networks, Electronics 10 (16) (2021) 2029, http://dx.doi.org/10.3390/electronics10162029.

[29] Z. Qin, Z. Zhang, Y. Li, J. Guo, Making deep neural networks robust to label noise: Cross-training with a novel loss function, IEEE Access 7 (2019) 130893–130902, http://dx.doi.org/10.1109/ACCESS.2019.2940653.

[30] Y. Xu, D. He, Q. Wang, H. Guo, Q. Li, Z. Xie, Y. Huang, An improved method of measuring wavefront aberration based on image with machine learning in free space optical communication, Sensors 19 (17) (2019) 3665, http://dx.doi.org/10.3390/s19173665.